Supporting Information for:

A Remarkably Simple Characterization of Glassy Carbon–Supported Films of Graphite, Graphene Oxide, and Chemically Converted Graphene Using $Fe(CN)_6^{3-}$/$Fe(CN)_6^{4-}$ and O_2 as Redox Probes

Fábio de Lima, Guilherme V. Fortunato, and Gilberto Maia[*]

Department of Chemistry, Universidade Federal de Mato Grosso do Sul, Caixa postal 549, Campo Grande, MS 79070-900, Brazil

*To whom correspondence should be addressed.

S1. Synthesis of Graphene Oxide (GO)

GO was synthesized[1] from natural graphite (GR) powder using a modified Hummers and Offeman[2] method, as originally proposed by Kovtyukhova et al.[3] GR powder (0.70 g, sized until 325 mesh, after smashing of graphite flakes from Aldrich) was added to a mixture of concentrated H_2SO_4 (Vetec, 2 mL), $K_2S_2O_8$ (Vetec, 0.37 g), and P_2O_5 (Vetec, 0.37 g). The solution was heated to 80 ºC using a hotplate and kept under stirring for 6 h using a magnetic stirrer. Successively, the solution was cooled to room temperature, added 20 mL of Milli-Q water, and allowed to stand overnight. The product was obtained by filtering in 0.22 µm nylon film and washed with Milli-Q water to remove the residual acid until neutral pH. The product was dried under room temperature.

The pre-oxidized graphite was then re-oxidized employing the Hummers and Offeman method.[2] Pretreated GR powder was added to cold (0 °C) concentrated H_2SO_4 (Vetec, 28 mL) containing $NaNO_3$ (Merck, 0.35 g). $KMnO_4$ (Nuclear, 2.10 g) was then gradually added under stirring and the temperature of the mixture was kept below 20 °C in an ice bath. Successively, the mixture was stirred at 35 °C using a hotplate and kept under stirring for 2 h employing a magnetic stirrer and then slowly diluted with Milli-Q water (120 mL), keeping the temperature below 50 °C. After that, the hotplate was switched off and 60 mL of Milli-Q water was added under stirring, followed by dilution with 220 mL of Milli-Q water. At this point the mixture was brownish grey. Shortly after it reached room temperature, 31 mL of 30% H_2O_2 was added dropwise to the mixture under magnetic stirring, and the color of the mixture changed into brilliant yellow, along with bubbling. The mixture was filtered and washed with 1:10 HCl (Merck):aqueous solution (100 mL) to remove metal ions, followed by washing with Milli-Q water in excess to remove the acid. The resulting solid was air-dried and diluted to make an graphite oxide dispersion (0.05% w/w) by ultrasonication. Exfoliation of graphite oxide to GO[4] was achieved by ultrasonication of the dispersion for 2 h.

S2. Synthesis of Chemically Converted Graphene (CCG)

CCG was synthesized employing the method proposed by Li et al.[4] The resulting 5.0 mL homogeneous dispersion of GO (0.05% w/w) was mixed with 5.0 mL of aqueous hydrazine sulfate solution (2.1 mg, Dinâmica) and 35.0 µl of ammonia solution (28 wt% in water, Vetec) in a 20-mL glass vial. After vigorously shaken for a few minutes, the vial was kept in a water bath (~95 ºC) for 2 h. Once reaching room temperature, the mixture was black. CCG was obtained after filtration under vacuum using 0.22 µm nylon film and washed with 0.5% v/v ammonia solution (50 mL). Excess ammonia was removed by washing with Milli-Q water

until neutral pH. Finally, CCG was dried under vacuum at room temperature.

S3. Raman Spectra of GR, GO, and CCG

Raman spectra were recorded from 440 to 4000 cm^{-1} on a Raman system (Senterra, Bruker) with excitation energy of 0.2 W (532 nm) (Figure S1). As shown in Figure S1, the first-order spectrum of pristine GR displays a prominent G band at ~1582 cm^{-1} (Table S1). The second-order (two-photon) spectrum of the starting GR sample is dominated by a shoulder (~2668 cm^{-1}) and a strong band at ~2717 cm^{-1} (2D band) (Table S1). The 2D band is the overtone (second harmonic) of the D band.[5] The D band is not present in defect-free graphite and its relative intensity increases with graphitic disorder—in graphitic materials the integrated intensity ratio of D and G bands (I_D/I_G) increases with the amount of disorder.[5]
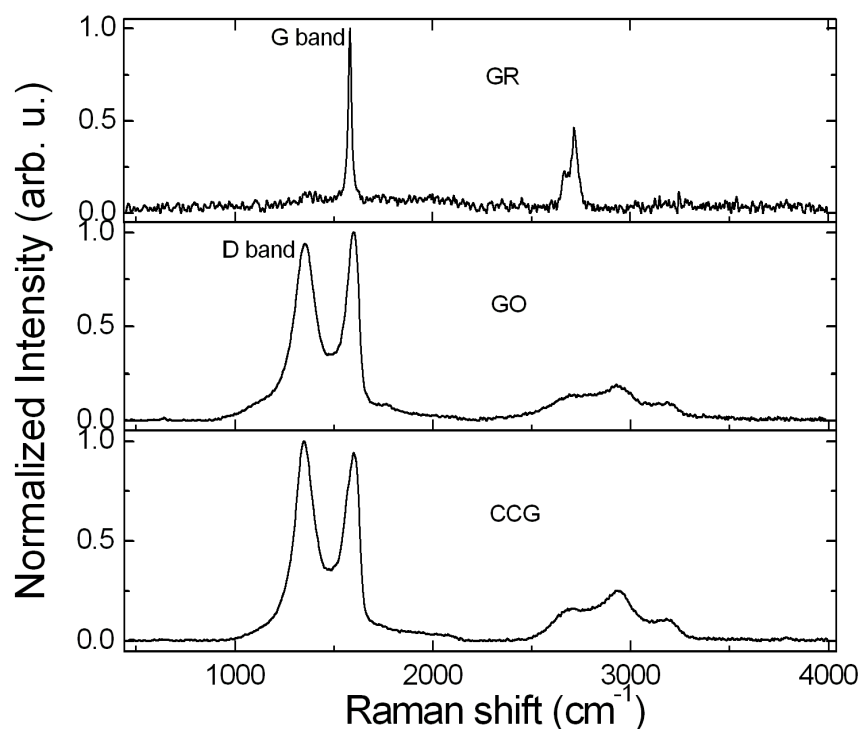

Figure S1. Raman spectra of GR, GO, and CCG recorded using 532 nm laser excitation. The integration time was 30 seconds for GR and 10 seconds for GO and CCG spectra.

Table S1. Raman peak positions.

Material	D band (cm^{-1})	G band (cm^{-1})	2D band	I_D/I_G (%)
GR		1582	2717	
GO	1354	1600	2940	0.93
CCG	1348	1600	2940	1.06

The spectrum of the GO material (Figure S1) reveals a prominent D band at ~1354 cm^{-1} and the presence of a G band at ~1600 cm^{-1} (Table S1); the I_D/I_G ratio increases dramatically in comparison with that of the starting GR material (from 0.0 to 0.93; Table S1), implying that the oxidation process proposed in topic 1 has introduced a considerable amount of structural disorder in the GO lattice.[5] The same conclusion can be drawn when the second-order spectrum is inspected. First, the 2D band is seen to broaden and decrease in relative intensity, compared with the G band—an effect that has been related to presence of defects in graphitic materials. Secondly, a band appears centered at 2940 cm^{-1}, partly obscuring the 2D band.[5] This new band results from the combination of the two modes that give rise to the first-order D and G bands and is caused by lattice disorder.[5] When the Raman spectrum of the CCG material (Figure S1) is compared with that of the GO sample (Figure S1), subtle changes are observed. The I_D/I_G ratio changes moderately (1.06 *vs.* 0.93 before reduction; Table S1) and the shape of the first-order spectrum is altered to some extent. The D band of the CCG material is somewhat more symmetrical relative to the D band of the GO material. Stankovich et al.[6] assumed that reduction increases the number of aromatic domains of smaller overall size in graphene, leading to enhancement of the I_D/I_G ratio.[5] Regarding the second-order spectrum, the 2D band appears more intense and defined than the band at 2940 cm^{-1} of the GO material (Figure S1). Paredes et al.[5] assumed that the carbon lattice in GO develops to some degree an amorphous character, due to the oxidation process itself. When the GO sheet is deoxygenated by the chemical reduction process, the distortion of the 6-fold aromatic rings is removed, and the carbon lattice returns to an essentially graphitic, but highly defective, state.[5] Similar changes upon chemical reduction of graphene oxide have been recently documented by other investigators,[1,5-9] even though in ref. 9 the band attributions are inverted. The Raman spectral results described above indicate that GO was well deoxygenated in CCG.

S4. Fourier Transform Infrared (FT-IR) Spectra of GR, GO, and CCG

FT-IR transmittance spectroscopy was performed with a Bomen MB100 spectrophotometer equipped with a liquid-nitrogen–cooled MCT detector (Quebec, Canada), using a KBr pellet. The successful confirmation of graphite oxidation to produce GO is illustrated in Figure S2.
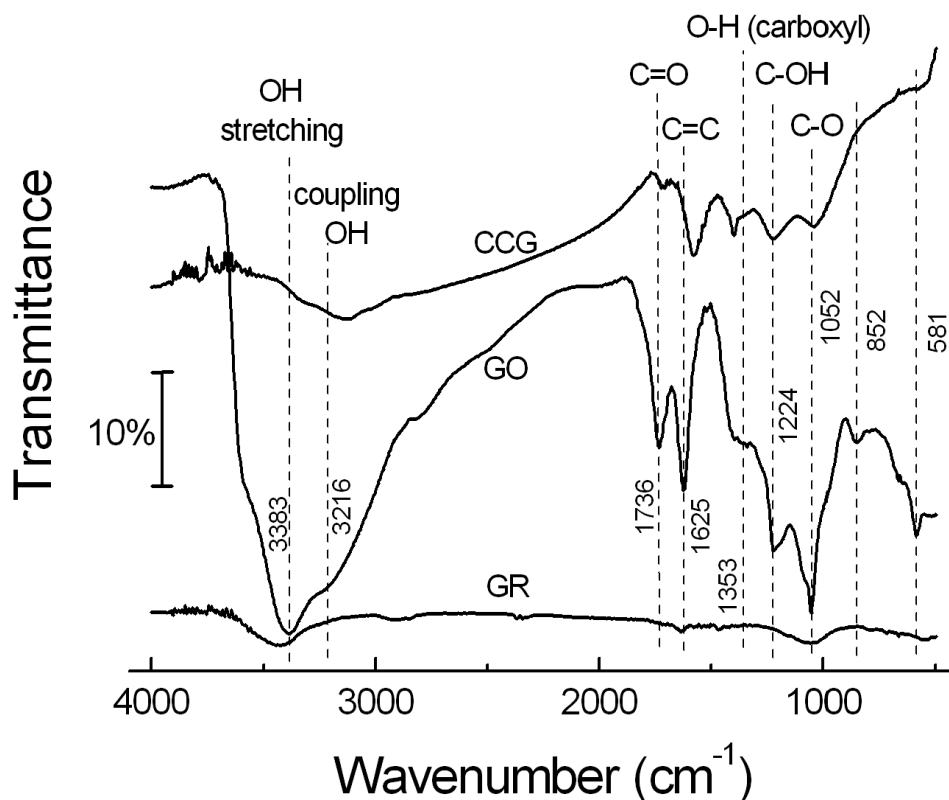
Figure S2. FT-IR spectra of GR, GO, and CCG.

The spectrum of GO shows a broad and intense peak of O-H groups[1] centered at ~3383 cm^{-1}, which could be attributed to the O-H stretching mode of intercalated water[8-10]; O-H (broad coupling ν(O-H)) at ~3216 cm^{-1} originated from carboxylic acid[8,10,11]; strong C=O peak attributed to carboxylic acid and carbonyl moieties (ν(carboxylic acid and carbonyl)) at 1736 cm^{-1};[1,8-11] skeletal vibrations (C=C) of the remnant sp^2 species (unoxidized graphitic domains) or contribution from the stretching deformation vibration of intercalated water at ~1625 cm^{-1};[1,8-11] O-H (ν(carboxyl))[8] and/or O-H in carbonyl[10] (O-H deformation peak)[1] at ~1353 cm^{-1}; C-OH stretching peak[1] or C-O vibrations[9] at 1224 cm^{-1}; and C-O (ν(epoxy or alkoxy or ether)) (C-O stretching peak) at ~1052 cm^{-1}.[1,8-11] After exfoliated GO is chemically reduced (CCG), the broad and intense peak corresponding to O-H stretching disappears, the broad coupling of OH is sufficiently decreased, the C=O vibration band disappears,[8] the peak at 1625 cm^{-1} is displaced to 1582 cm^{-1} (sp^2-hybridized C=C (in-plane stretching, ~1550-1650 cm^{-1}))[12], and the transmittance bands of oxygen functionalities are sufficiently decreased,[8,11] indicating the high purity of the CCG thus produced.[8,11]

S5. Thermogravimetric Analysis (TGA) of GR, GO, and CCG

TGA was performed using a Q50 thermogravimetric analyzer (TA Instruments) on samples sized 4 to 6 mg, under N_2 gas flow (60 mL min^{-1}), over temperatures ranging from ambient to 900 °C at a heating rate of 10 °C min^{-1}, and employing Pt crucibles. Figure S4 displays TGA thermograms showing mass loss as a function of temperature for GR, GO, and CCG.
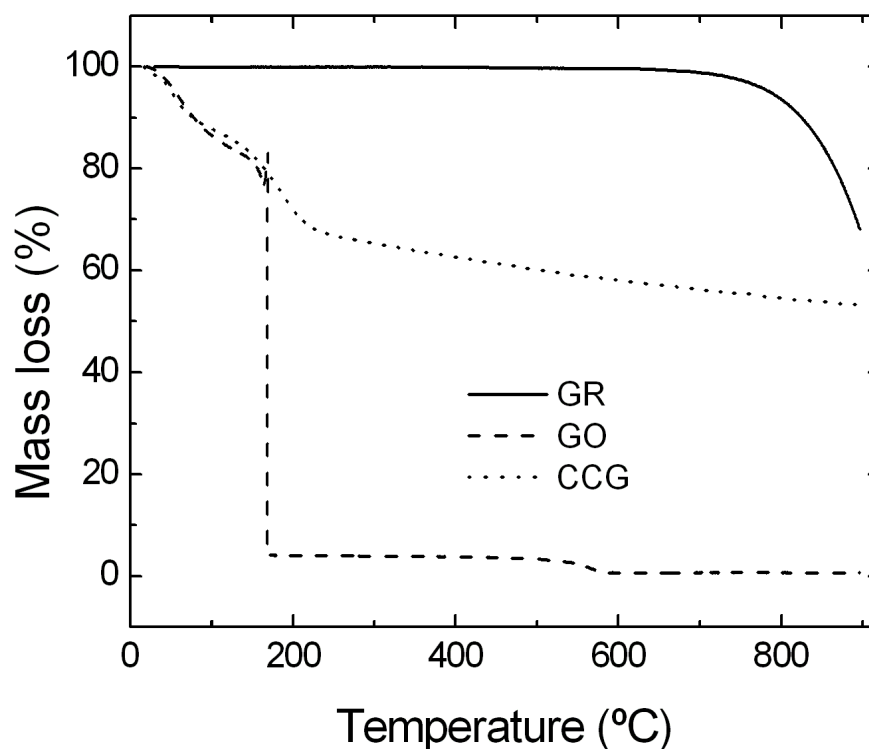

Figure S3. Decomposition behavior of GR, GO, and CCG.

As depicted in Figure 3, the GR sample showed mass loss (~30%) above 700 °C. The GO sample starts to lose mass (~13%) even earlier, below 100 °C, a behavior that can be ascribed to removal of adsorbed water[5] (elimination of interlamellar water)[7]. With GO, sudden mass loss occurs at ~167 °C, presumably due to pyrolysis of labile oxygen-containing functional groups, yielding CO, CO_2, and steam.[5-7] Thermal decomposition of GO can be accompanied by vigorous release of gas, resulting in rapid thermal expansion of the material.[6] This is evident through a much larger mass loss, to nearly zero (caused by flying GO debris in the TGA instrument), during a rapid heating regime.[6] On the other hand, the CCG sample showed much higher thermal stability, due to a decrease in thermally labile oxygen functional groups (deoxygenation)[7] by chemical reduction with hydrazine. Apart from mass loss (~20%) similar to GO until ~167 °C (Figure S3), CCG subsequently underwent no more than ~10% mass loss

until ~217 ºC, suggesting that the labile oxygen functional groups in GO are largely removed by reaction with hydrazine.[5] For CCG, slow mass loss (of just ~16%), was detected above ~217 °C up to 900 °C, implying that the more stable oxygen functionalities are not completely eliminated from CCG by chemical reduction.[5,6,9]

S6. X-ray Photoelectron Spectroscopy (XPS) Analysis of GR, GO, and CCG

XPS measurements were performed using an Mg K_α source (XR50, Specs GmbH) and a hemispherical electron energy analyzer (Phoibos 100, Specs GmbH). A two-point calibration of the energy scale was performed using sputter-cleaned gold (Au $4f_{7/2}$, binding energy (BE) = 84.00 eV) and copper (Cu $2p_{3/2}$, BE = 932.67 eV) samples. Figure S4 presents the C 1s spectra of GO and CCG samples.
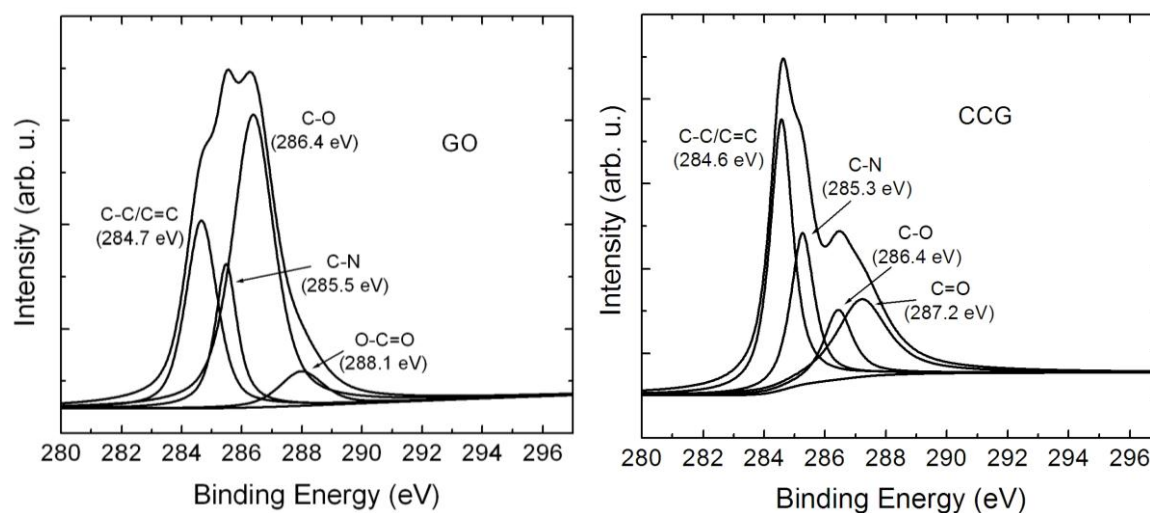
Figure S4. Deconvoluted C 1s XPS spectra of GO and CCG.

The deconvoluted C 1s spectrum of GO (Figure S4) exhibits four types of carbon bond, located at 284.7 eV (graphitic C=C and/or C-C species)[1,5-7,9-11], 285.5 eV (C-N species)[6,10], 286.4 eV (C-O species)[1,5-7,9-11], and 288.1 eV (O-C=O species)[1,5-7,9-11]. For CCG, the C 1s XPS spectrum (Figure S4) exhibits three types of carbon bond similar to those of GO, in addition to one different type, located at 284.6, 285.3, 286.4, and 287.2 eV (C=O species)[1,5-7,10]. However, peak intensities of oxide species are much weaker than in the GO spectrum, suggesting considerable deoxygenation by the reduction process.[1,5-7,10] The increased peak intensity at 285.3 eV reinforces nitrogen incorporation during reduction.[1,5,6] Evidence for deoxygenation of GO nanosheets by the chemical reduction process was also provided by the O/C and N/C atomic ratios derived from XPS survey spectra (not shown), which yielded values of 0.35 and

0.01 for the GO material and 0.27 and 0.03 for the CCG material, respectively. The residual oxygen functionalities retained following reduction would still render the nanosheets somewhat hydrophilic, imparting them with colloidal stability in water, and also explaining the significant amount of water that this material is able to adsorb[5] (see TGA results, Figure S3).

S7. Scanning Electron Microscopy (SEM) Images of GR, GO, and CCG

The microstructures of GR, GO and CCG were visually characterized by SEM, which was performed on a JEOL JSM-6380LV field-emission scanning electron microscope using an accelerating voltage of 30 kV. Figure S5 shows SEM images acquired *ex situ* for GR, GO, and CCG.
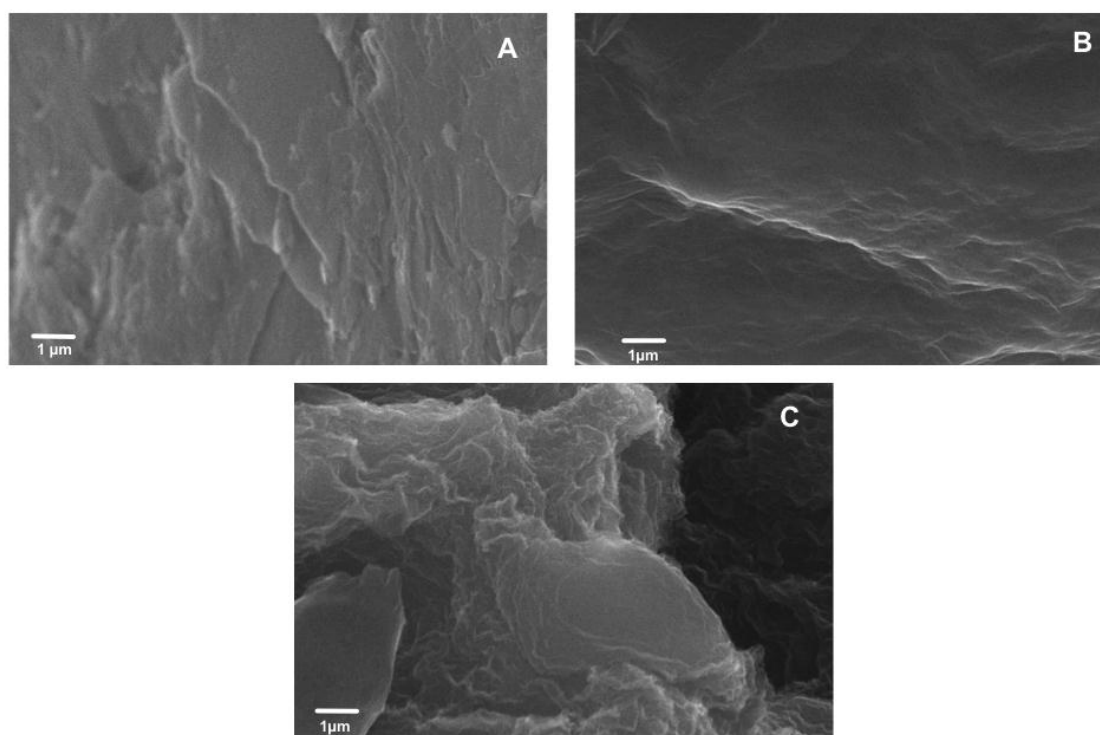
Figure S5. SEM images of GR (A), GO (B), and CCG (C). 10 000× magnification.

The SEM image of GR (Figure S5A) suggests that GR is constituted of large and extended lamellae, in agreement with the SEM image shown by Allen et al.[13] The SEM image of GO (Figure S5B) reveals an overall much smoother surface containing gentle hills, while CCG (Figure S5C) displays very thin lamellar aggregates, in agreement with SEM images from the literature.[1,6,14-17]

S8. Schematic chemical structures of GR, GO, and CCG based on chemical functionalities identified by Raman, FT-IR, and XPS
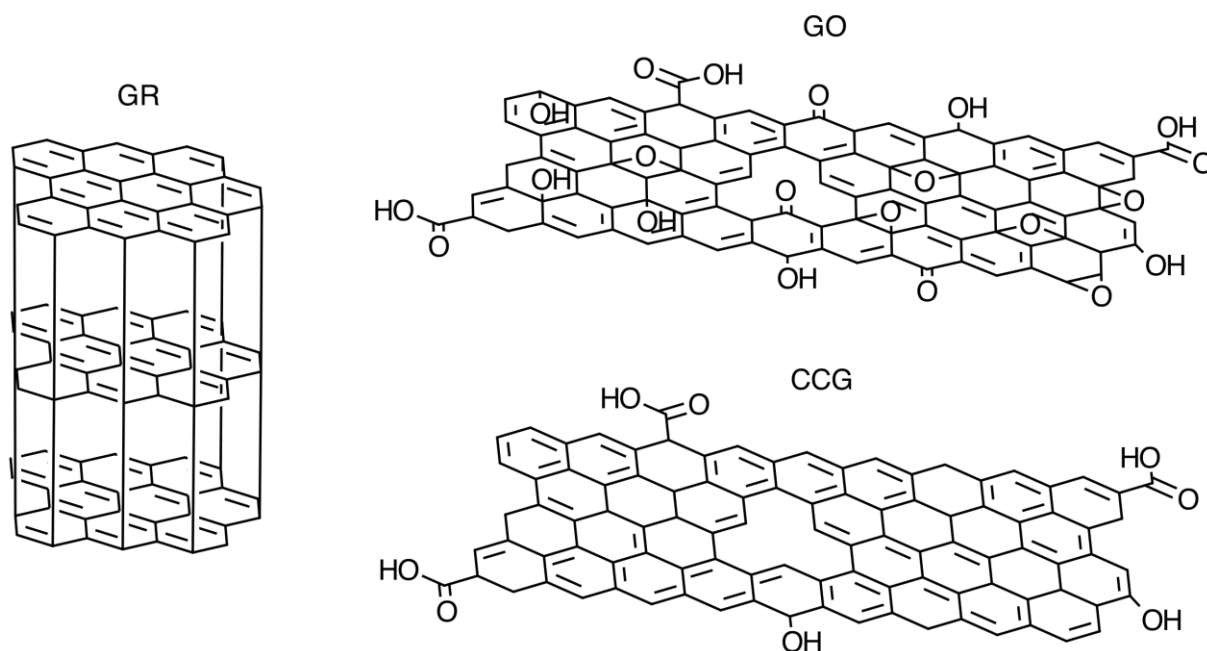
Figure S6. Probable chemical structures of GR, GO, and CCG.

S9. CV Responses from Bare GC, GC/GR, GC/GO, and GC/CCG Electrodes in an N_2-Saturated 1 M KCl Solution Containing a Total 10 mM Concentration of $K_3[Fe(CN)_6]/K_4[Fe(CN)_6]$ (1:1 Molar Ratio)

The main characteristics of an electrochemical reversible (Nernstian) system observed in the experiments during cyclic voltammetric experiments (reversible wave) were: peak potential separation close to 60/n mV (25 °C), regardless of scan rate; chemical stability of the reduced form, demonstrated by a peak current ratio of 1, and I_p (as well as the current at any other point on the wave) proportional to $v^{1/2}$, intercepting the origin by extrapolation—a characteristic feature of Nernstian waves of diffusing species.[18] As we initially used $K_3[Fe(CN)_6]/K_4[Fe(CN)_6]$ (total 10 mM concentration, 1:1 molar ratio) as the redox probe—an expected Nernstian system—we checked mainly the influence of electrode surface on the expected Nernstian behavior, since the influence of some impurities of the medium are repeatable in all the experiments. In the case of a Nernstian system[18]:

$$I_p = (2.69 \times 10^5)n^{3/2}AD_R^{1/2}C_R^*v^{1/2} \qquad (S1)$$

where n is the number of transferred electrons, A is the electrochemically active surface area (*ECSA*), D_R is the diffusion coefficient of reduced species, and C_R^* is the bulk reduced species concentration (the opposite meaning is applied to oxidized specie). Thus, if n, D_R, and C_R^* are known, the slopes of I_p *vs.* $v^{1/2}$ (see insets A to Figures S7-S14), which are linear and intercept the origin by extrapolation, allow us to determine *ECSA*. In the present case, for K$_4$[Fe(CN)$_6$] (cathodic branch) for example, n equaled 1, D_R was assumed equal to 6.67×10^{-6} cm^2 s^{-1},[19] and C_R^* was 5 mM.

Cyclic voltammogram curves normalized by *ECSA* (Table S2) are shown in Figures S7-S14. The GC electrode response (Figure S7) is characteristic of Fe(CN)$_6^{3-}$/Fe(CN)$_6^{4-}$ redox probes on bare GC,[20-22] with redox peaks centered at 0.22 V. The $I_{p\ anodic}/I_{p\ cathodic}$ ratio approaches 1 when the potential scan rate is increased (see inset A to Figure S7). However, peak potential separation approaches 70 mV only at a low potential scan rate (inset B to Figure S7). This type of response may suggest a quasi-reversible behavior[18] of Fe(CN)$_6^{3-}$/Fe(CN)$_6^{4-}$, not intrinsic to the nature of these redox probes, but possibly caused by a surface effect of the GC electrode coupled with some salt impurities.
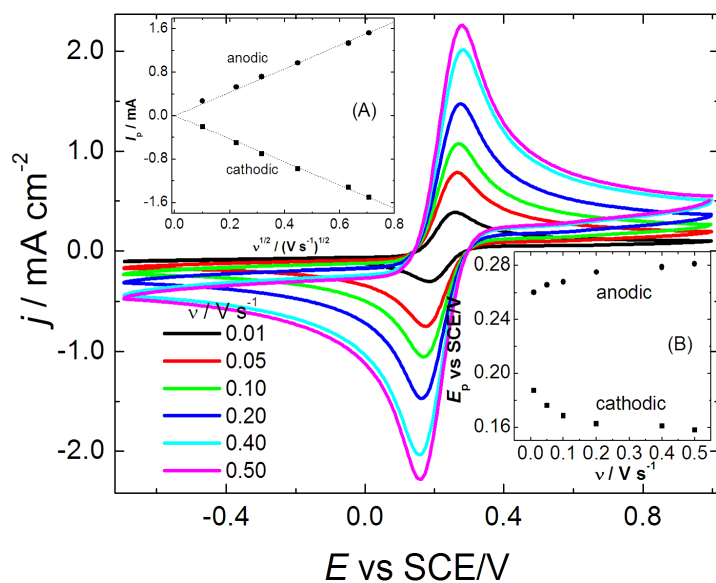
Figure S7. Cyclic voltammograms for a bare GC electrode in N$_2$-saturated 1 M KCl solution containing a total 10 mM concentration of K$_3$[Fe(CN)$_6$]/K$_4$[Fe(CN)$_6$] (1:1 molar ratio). Insets: Anodic and cathodic peak currents *vs.* square root potential scan rate (A) and anodic and cathodic peak potentials *vs.* potential scan rate (B) for the same electrode and conditions. Scans start at 1.0 V.

The redox peaks are centered at 0.20 V for the GC/GR electrode (Figure S8), with an $I_{p\ anodic}/I_{p\ cathodic}$ ratio approaching 1 when the potential scan rate is increased (see inset A to Figure S8). However, peak potential separation approaches 90 mV only at a low potential scan

rate (inset B to Figure S8). These responses enhance the surface effect of the GC/GR electrode on $Fe(CN)_6^{3-}/Fe(CN)_6^{4-}$ redox behavior, since the only difference between the results obtained with the GC/GR electrode (Figure S8) and the bare GC electrode (Figure S7) is the presence of a GR film containing 8.0 µg cm^{-2} of GR on the GC surface. Notice that *ECSA* decreased from 0.61 cm^2 (bare GC) to 0.42 cm^2 (GC/GR) (Table S2).
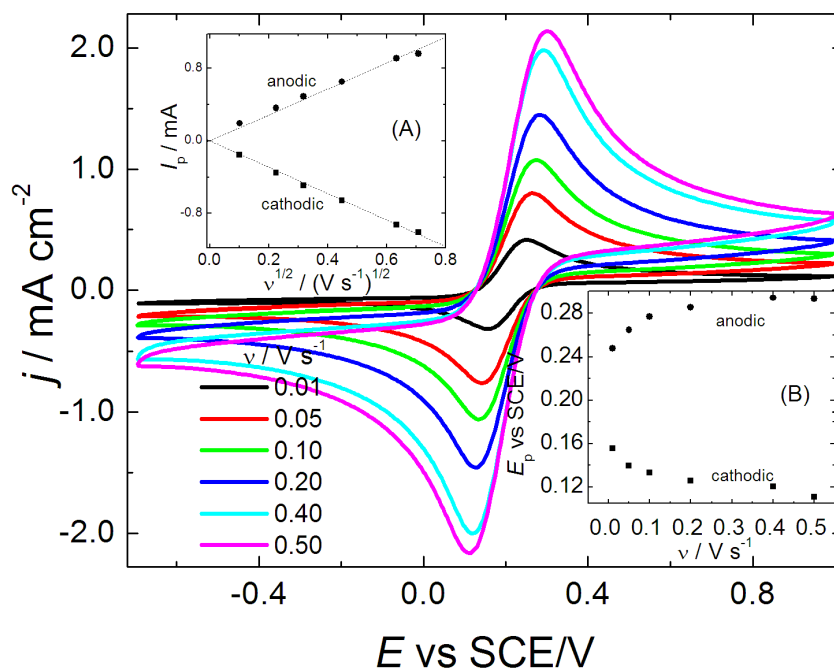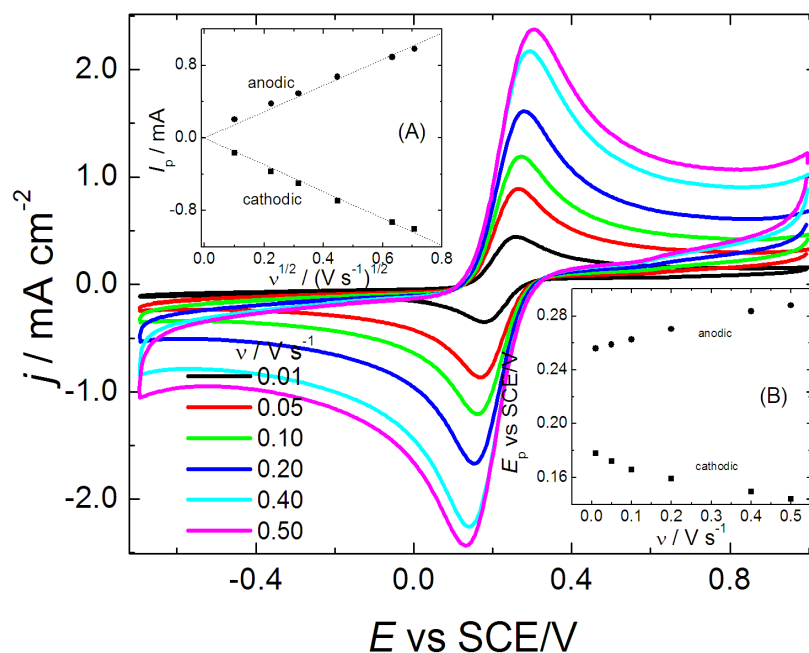

Figure S8. Cyclic voltammograms for a GC/GR electrode (8.0 µg cm^{-2} of GR on the GC surface) in N_2-saturated 1 M KCl solution containing a total 10 mM concentration of $K_3[Fe(CN)_6]/K_4[Fe(CN)_6]$ (1:1 molar ratio). Inset: Anodic and cathodic peak currents *vs.* square root potential scan rate (A) and anodic and cathodic peak potentials *vs.* potential scan rate (B) for the same electrode and conditions. Scans start at 1.0 V.

Redox peaks are centered at 0.22 V for the GC/GO electrode (Figure S9), with an $I_{p\,anodic}/I_{p\,cathodic}$ ratio approaching 1 when the potential scan rate is increased (see inset A to Figure S9). However, peak potential separation approaches 100 mV only at a low potential scan rate (inset B of Figure S9), enhancing the strong surface effect of the GC/GO electrode on $Fe(CN)_6^{3-}/Fe(CN)_6^{4-}$ redox behavior, relative to bare GC and GC/GR electrodes. Notice that *ECSA* was sufficiently decreased for GC/GO (to 0.29 cm^2) in relation to bare GC and GC/GR (0.61 and 0.42 cm^2, respectively) (see Table S2).
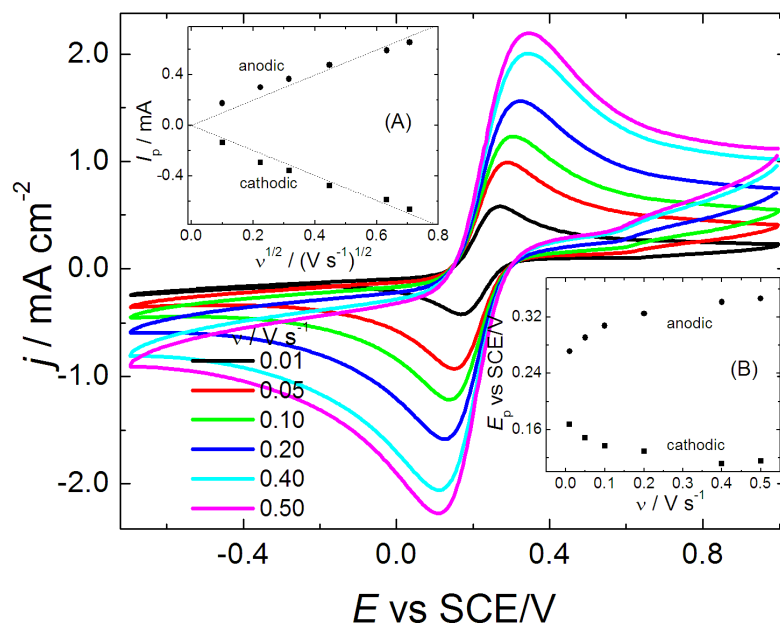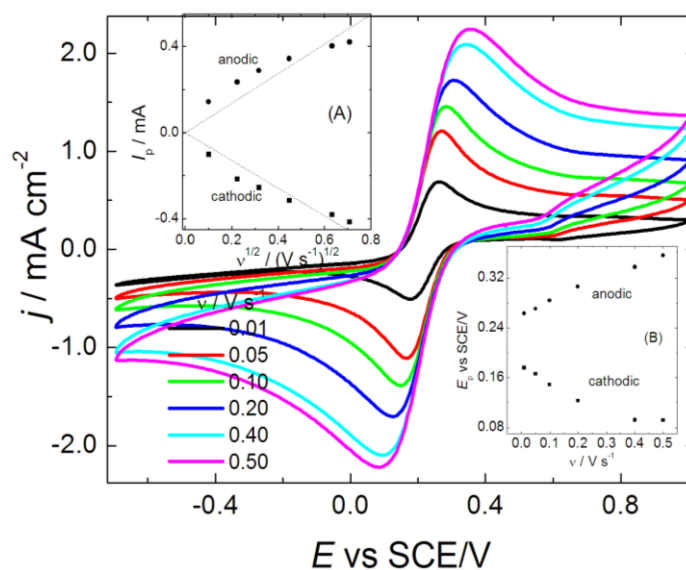
Figure S9. Cyclic voltammograms for a GC/GO electrode (8.0 µg cm^{-2} of GO on the GC surface) in N$_2$-saturated 1 M KCl solution containing a total 10 mM concentration of K$_3$[Fe(CN)$_6$]/K$_4$[Fe(CN)$_6$] (1:1 molar ratio). Inset: Anodic and cathodic peak currents *vs.* square root potential scan rate (A) and anodic and cathodic peak potentials *vs.* potential scan rate (B) for the same electrode and conditions. Scans start at 1.0 V.

Redox peaks are centered at 0.22 V for the GC/CCG electrode (Figure S10), with an I_p anodic/I_p cathodic ratio approaching 1 when the potential scan rate is increased (see inset A to Figure S10). However, peak potential separation nears 75 mV only at a low potential scan rate (inset B to Figure S10), approaching the surface effect of the GC/CCG electrode on Fe(CN)$_6^{3-}$/Fe(CN)$_6^{4-}$ redox behavior relative to bare GC, even though *ECSA* decreased (to 0.43 cm^2) in relation to bare GC (0.61 cm^2) (see Table S2).

Figure S10. Cyclic voltammograms for a GC/CCG electrode (8.0 μg cm^{-2} of CCG on the GC surface) in N$_2$-saturated 1 M KCl solution containing a total 10 mM concentration of K$_3$[Fe(CN)$_6$]/K$_4$[Fe(CN)$_6$] (1:1 molar ratio). Inset: Anodic and cathodic peak currents *vs.* square root potential scan rate (A) and anodic and cathodic peak potentials *vs.* potential scan rate (B) for the same electrode and conditions. Scans start at 1.0 V.

When the loading amount of GO or CCG on the GC surface is increased 10 times (80 μg cm^{-2}) (Figures S11 and S12), redox peaks are centered at 0.22 V for GC/GO and GC/CCG (Figures S11 and S12), with $I_{p \, anodic}/I_{p \, cathodic}$ ratios approaching 1 when the potential scan rate is increased (see insets A to Figures S11 and S12). For the GC/GO electrode, I_p intercepting the origin by extrapolation is not as proportional to $v^{1/2}$ (see inset A to Figure S11). In addition, peak potential separation approaches 85 mV only at a low potential scan rate (inset B to Figure S11), making the surface effect of GC/GO electrode on Fe(CN)$_6^{3-}$/Fe(CN)$_6^{4-}$ redox behavior differ from that exerted by bare GC. Also, *ECSA* decreased sufficiently (to 0.19 cm^2) in relation to bare GC (0.61 cm^2) (see Table S2). For GC/CCG, even though peak potential separation approached 60 mV at a low potential scan rate (inset B to Figure S12), the capacitive current densities reach high values, of up to −4.0 mA cm^{-2} at −0.70 V and 500 mV s^{-1}, making the surface effect of the GC/CCG electrode on Fe(CN)$_6^{3-}$/Fe(CN)$_6^{4-}$ redox behavior differ from that exerted by bare GC. Also, *ECSA* decreased (to 0.45 cm^2) in relation to bare GC (0.61 cm^2) (see Table S2).
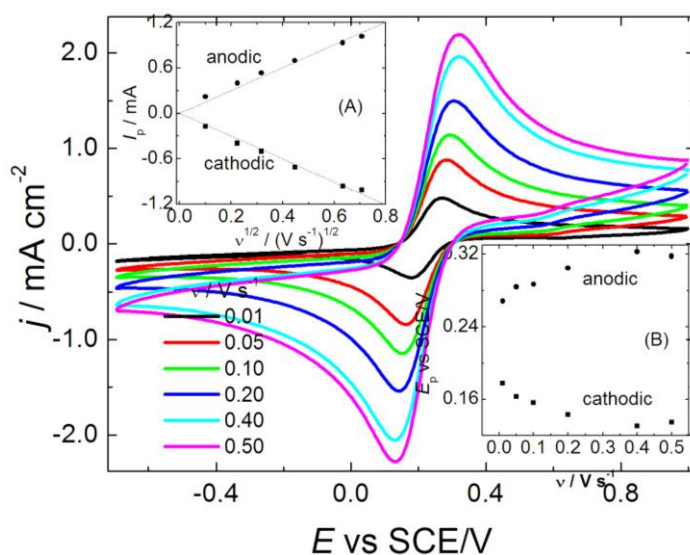
Figure S11. Cyclic voltammograms for a GC/GO electrode (80 µg cm^{-2} of GO on the GC surface) in N$_2$-saturated 1 M KCl solution containing a total 10 mM concentration of K$_3$[Fe(CN)$_6$]/K$_4$[Fe(CN)$_6$] (1:1 molar ratio). Inset: Anodic and cathodic peak currents *vs.* square root potential scan rate (A) and anodic and cathodic peak potentials *vs.* potential scan rate (B) for the same electrode and conditions. Scans start at 1.0 V.
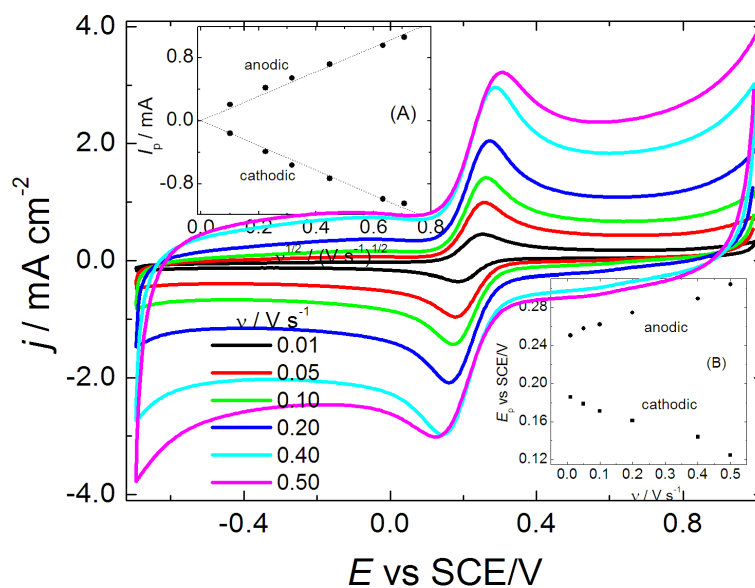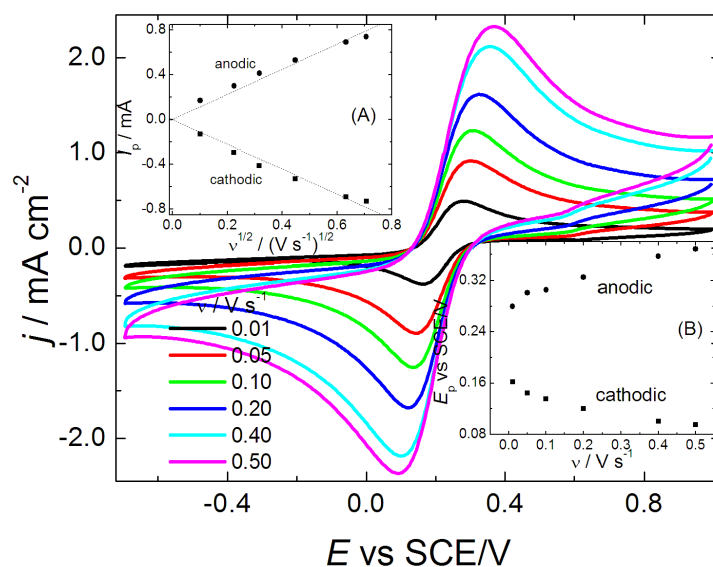

Figure S12. Cyclic voltammograms for a GC/CCG electrode (80 µg cm^{-2} of CCG on the GC surface) in N$_2$-saturated 1 M KCl solution containing a total 10 mM concentration of K$_3$[Fe(CN)$_6$]/K$_4$[Fe(CN)$_6$] (1:1 molar ratio). Inset: Anodic and cathodic peak currents *vs.* square root potential scan rate (A) and anodic and cathodic peak potentials *vs.* potential scan rate plot (B) for the same electrode and conditions. Scans start at 1.0 V.

When the loading amount of GO or CCG is decreased 4 times (2 µg cm^{-2}) in relation to 8 µg cm^{-2} (Figures S13 and S14), the redox peaks are also centered at 0.22 V for GC/GO and GC/CCG (Figures S13 and S14), with $I_{p\ anodic}/I_{p\ cathodic}$ ratios approaching 1 when the potential scan rate is increased (see insets A to Figures S13 and S14). For the GC/GO electrode, peak potential separation approaches 90 mV only at a low potential scan rate (inset B to Figure S13), making the surface effect of the GC/GO electrode on $Fe(CN)_6^{3-}/Fe(CN)_6^{4-}$ redox behavior differ from that exerted by bare GC. Also, $ECSA$ decreased (to 0.44 cm^2) in relation to bare GC (0.61 cm^2) (see Table S2). For GC/CCG, peak potential separation approaches 120 mV at a low potential scan rate (inset B to Figure S14), making the surface effect of this electrode on $Fe(CN)_6^{3-}/Fe(CN)_6^{4-}$ redox behavior differ from that exerted by bare GC. Also, $ECSA$ decreased (to 0.32 cm^2) in relation to bare GC (0.61 cm^2) (see Table S2).

Figure S13. Cyclic voltammograms for a GC/GO electrode (2 µg cm^{-2} of GO on the GC surface) in N_2-saturated 1 M KCl solution containing a total 10 mM concentration of $K_3[Fe(CN)_6]/K_4[Fe(CN)_6]$ (1:1 molar ratio). Inset: Anodic and cathodic peak currents *vs.* square root potential scan rate (A) and anodic and cathodic peak potentials *vs.* potential scan rate (B) for the same electrode and conditions. Scans start at 1.0 V.

Figure S14. Cyclic voltammograms for a GC/CCG electrode (2 $\mu g\ cm^{-2}$ of CCG on the GC surface) in N_2-saturated 1 M KCl solution containing a total 10 mM concentration of $K_3[Fe(CN)_6]/K_4[Fe(CN)_6]$ (1:1 molar ratio). Inset: Anodic and cathodic peak currents *vs.* square root potential scan rate (A) and anodic and cathodic peak potentials *vs.* potential scan rate (B) for the same electrode and conditions. Scans start at 1.0 V.

Table S2. *ECSA* values for modified GC electrodes, calculated using Eq. S1 in addition to I_p cathodic values shown in insets A to Figures S7-S14. The *ECSA* value for bare GC, calculated using Eq. S1 in addition to $I_{p\ cathodic}$ values shown in inset A to Figure S7, is 0.61 cm^2.

Loading amount of modifier ($\mu g\ cm^{-2}$)	*ECSA* of modified electrode (cm^2)		
	GC/GR	GC/GO	GC/CCG
80	0.47	0.19	0.45
8.0	0.42	0.29	0.43
2.0	0.43	0.44	0.32
0.04	0.50	0.53	0.43
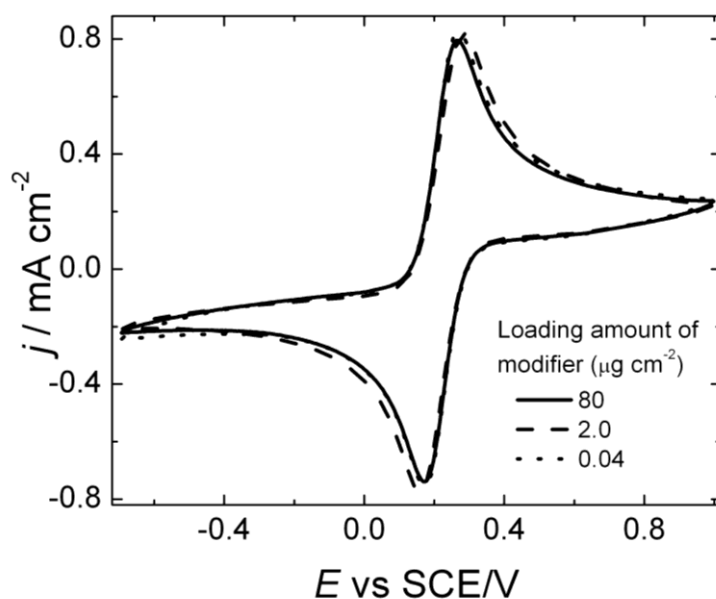
Figure S15. Cyclic voltammograms obtained in N_2-saturated 1 M KCl containing a total 10 mM concentration of $K_3[Fe(CN)_6]/K_4[Fe(CN)_6]$ (1:1 molar ratio) for GC electrodes surface-modified with GR. $v = 50$ mV s^{-1}. Scans start at 1.0 V.
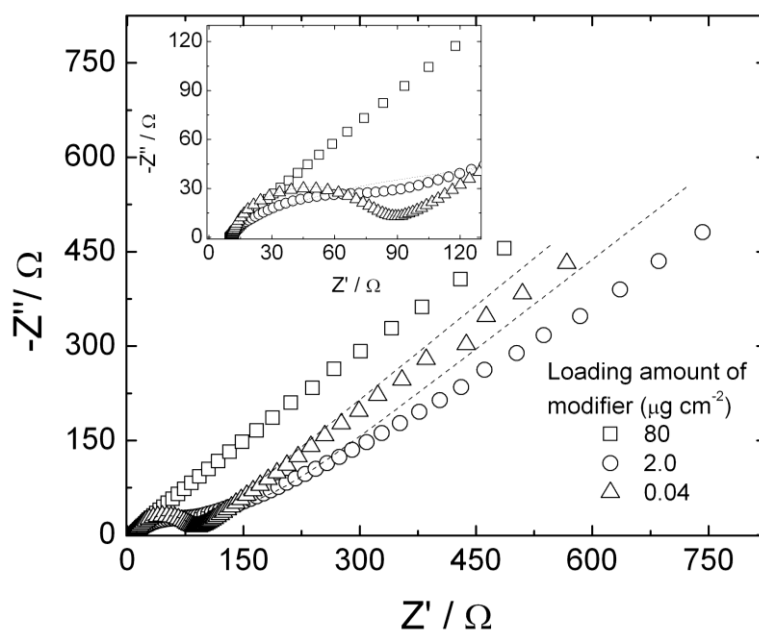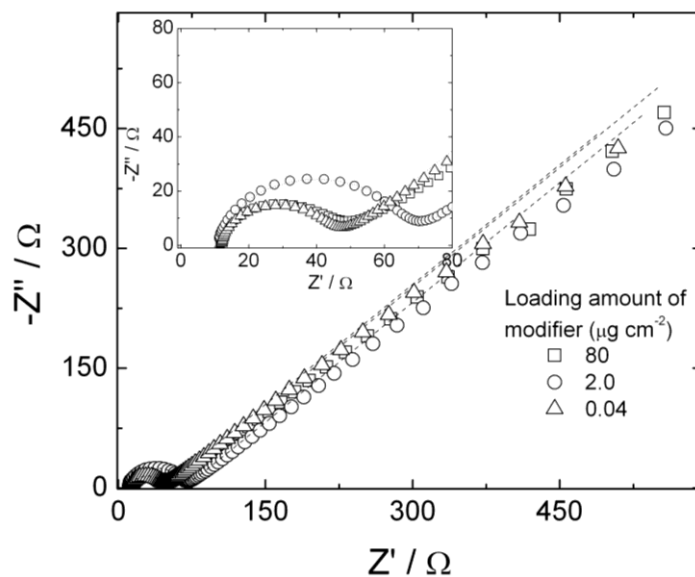

Figure S16. Impedance plane plots obtained in N_2-saturated 1 M KCl solution containing a total 10 mM concentration of $K_3[Fe(CN)_6]/K_4[Fe(CN)_6]$ (1:1 molar ratio) for GC electrodes surface-modified with different loading amounts of CCG. Potential perturbation: 25 mV (rms). Frequency range: 100 kHz–10 mHz. Constant potential for EIS acquisition: OCP (0.22 V vs. SCE on average). Lines represent spectra (adjusted) calculated using a non-linear least-squares program, conforming to the equivalent circuit $R_s[Q_{dl}(R_{ct}W_{lf})]$, or $R_s[Q_{dl}(R_{ct}Q_{lf})]$. Calculated average values: $R_s = 10$ Ω, $Q_{dl} = 10$ μF s^{n-1}, $n = 0.85$, and $W_{lf} = 5.0$ mF. Inset: Impedance plane plots restricted to 130 Ω in the main graph.
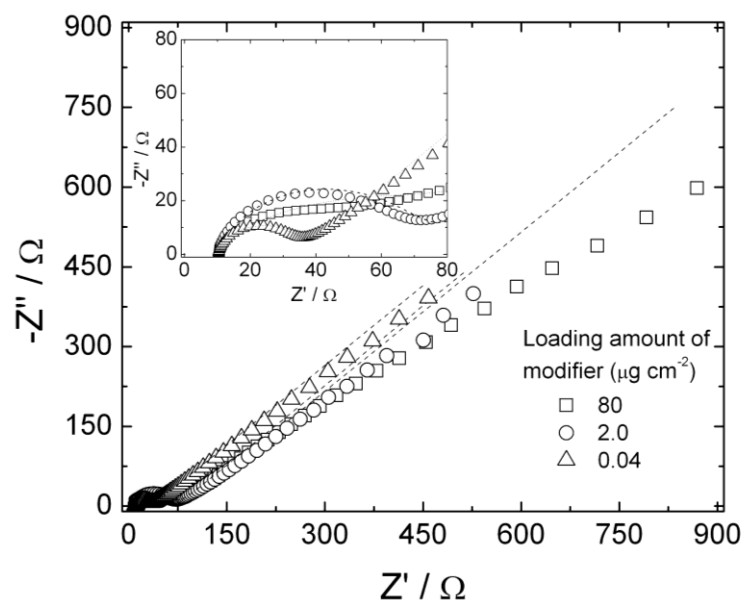
Figure S17. Impedance plane plots obtained in N_2-saturated 1 M KCl solution containing a total 10 mM concentration of $K_3[Fe(CN)_6]/K_4[Fe(CN)_6]$ (1:1 molar ratio) for GC electrodes surface-modified with different loading amounts of GO. Potential perturbation: 25 mV (rms). Frequency range: 100 kHz–10 mHz. Constant potential for EIS acquisition: OCP (0.22 V $vs.$ SCE on average). Lines represent spectra (adjusted) calculated using a non-linear least-squares program, conforming to the equivalent circuit $R_s[Q_{dl}(R_{ct}W_{lf})]$, or $R_s[Q_{dl}(R_{ct}Q_{lf})]$. Calculated average values: $R_s = 10\ \Omega$, $Q_{dl} = 10\ \mu F\ s^{n-1}$, $n = 0.85$, and $W_{lf} = 5.5$ mF. Inset: Impedance plane plots restricted to 80 Ω in the main graph.

Figure S18. Impedance plane plots obtained in N_2-saturated 1 M KCl solution containing a total 10 mM concentration of $K_3[Fe(CN)_6]/K_4[Fe(CN)_6]$ (1:1 molar ratio) for GC electrodes surface-modified with different loading amounts of GR. Potential perturbation: 25 mV (rms). Frequency range: 100 kHz–10 mHz. Constant potential for EIS acquisition: OCP (0.22 V $vs.$ SCE on average). Lines represent spectra (adjusted) calculated using a non-linear least-squares program, conforming to the equivalent circuit $R_s[Q_{dl}(R_{ct}W_{lf})]$, or $R_s[Q_{dl}(R_{ct}Q_{lf})]$. Calculated average values: $R_s = 10\ \Omega$, $Q_{dl} = 7\ \mu F\ s^{n-1}$, $n = 0.9$, and $W_{lf} = 6.0$ mF. Inset: Impedance plane plots restricted to 80 Ω in the main graph.
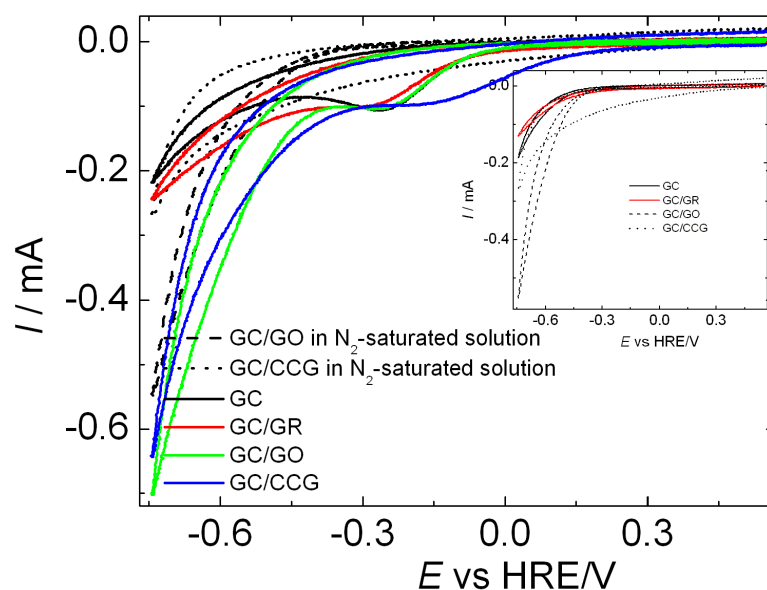
Figure S19. Cyclic voltammograms obtained in N_2- or O_2-saturated 0.1 M $HClO_4$ for a bare GC electrode and GC electrodes surface-modified with 8 μg cm^{-2} of GR or GO, or CCG. ν = 50 mV s^{-1}. Inset: Cyclic voltammograms obtained in N_2-saturated 0.1 M $HClO_4$ for a bare GC electrode and GC electrodes surface-modified with 8 μg cm^{-2} of GR or GO, or CCG. ν = 50 mV s^{-1}. Scans start at 0.55 V.
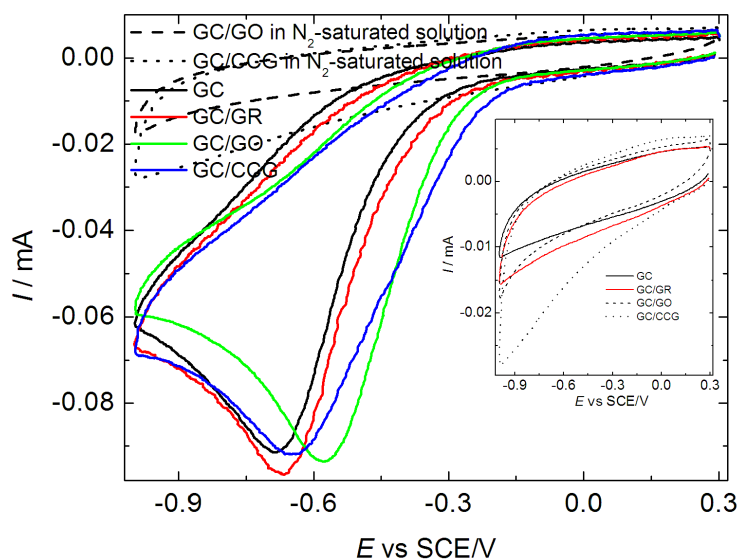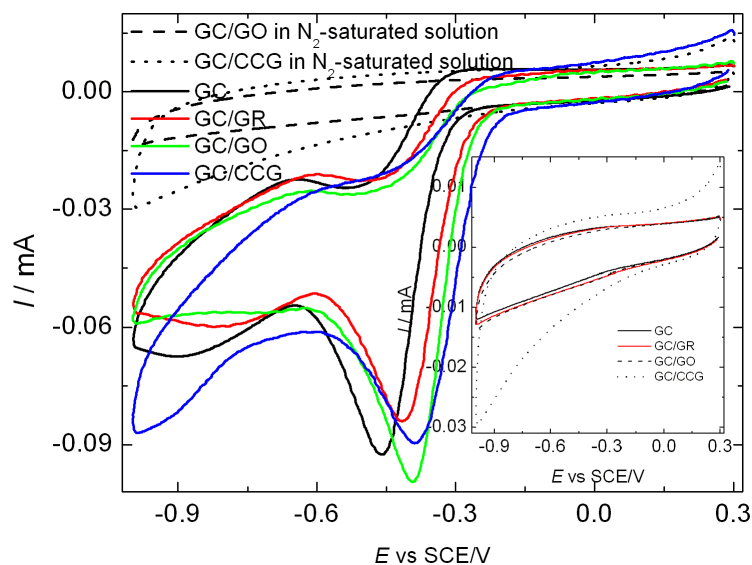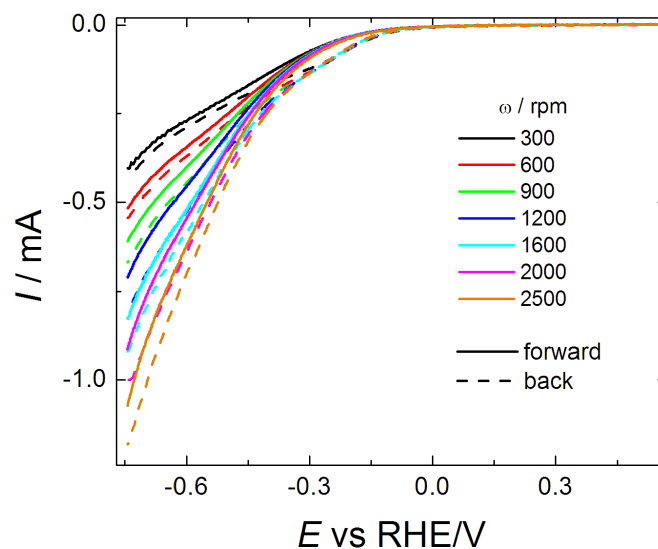

Figure S20. Cyclic voltammograms obtained in N_2- or O_2-saturated 0.1 M KH_2PO_4 (pH 7.0) for a bare GC electrode and GC electrodes surface-modified with 8 μg cm^{-2} μg of GR or GO, or CCG. ν = 50 mV s^{-1}. Inset: Cyclic voltammograms obtained in N_2-saturated 0.1 M KH_2PO_4 (pH 7.0) for a bare GC electrode and GC electrodes surface-modified with 8 μg cm^{-2} of GR or GO, or CCG. ν = 50 mV s^{-1}. Scans start at 0.30 V.

Figure S21. Cyclic voltammograms obtained in N_2- or O_2-saturated 0.1 M KOH for a bare GC electrode and GC electrodes surface-modified with 8 μg cm^{-2} of GR or GO, or CCG. Room temperature; ν = 50 mV s^{-1}. Inset: Cyclic voltammograms for a bare GC electrode and GC electrodes surface-modified with 8 μg cm^{-2} of GR or GO, or CCG. ν = 50 mV s^{-1}. Scans start at 0.30 V.

Figure S22. Hydrodynamic voltammetry curves for O_2 reduction on a bare GC electrode in O_2-saturated 0.1 M HClO$_4$. ν = 10 mV s^{-1}. Scans start at −0.75 V.
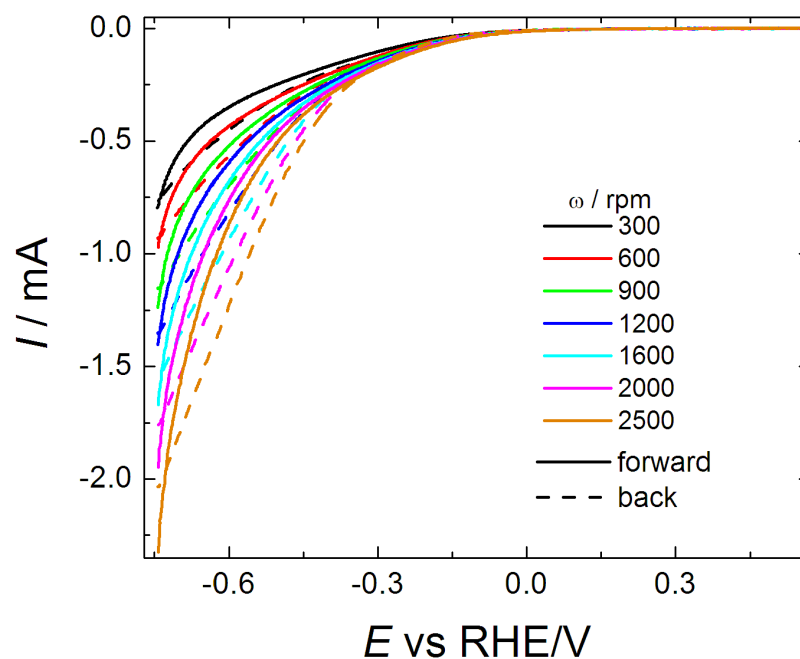
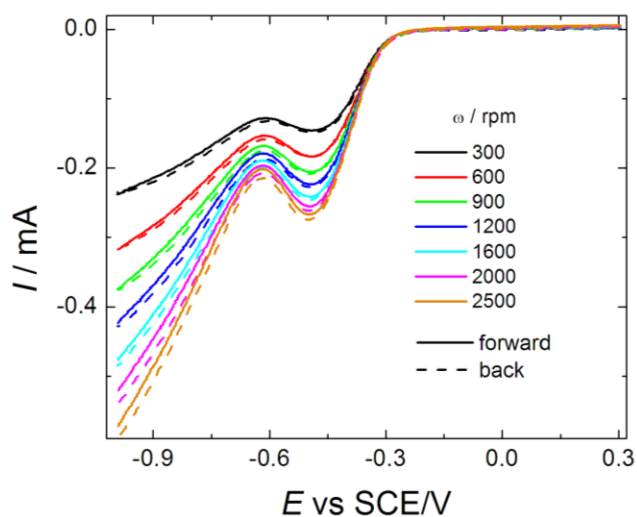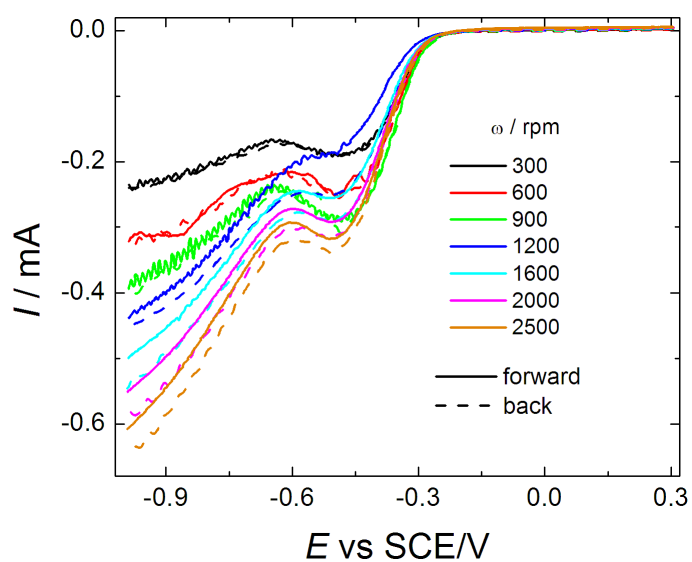Figure S23. Hydrodynamic voltammetry curves obtained in O_2-saturated 0.1 M $HClO_4$ for O_2 reduction on a GC electrode surface-modified with 8 µg cm^{-2} of GO. ν = 10 mV s^{-1}. Scans start at −0.75 V.
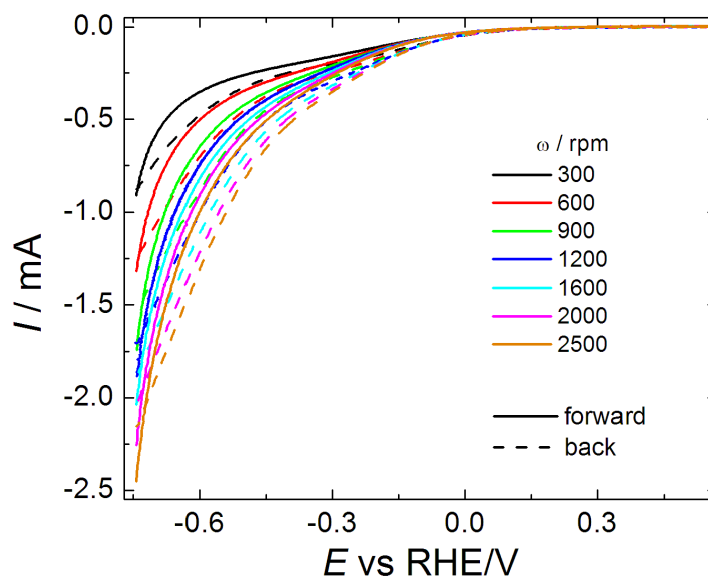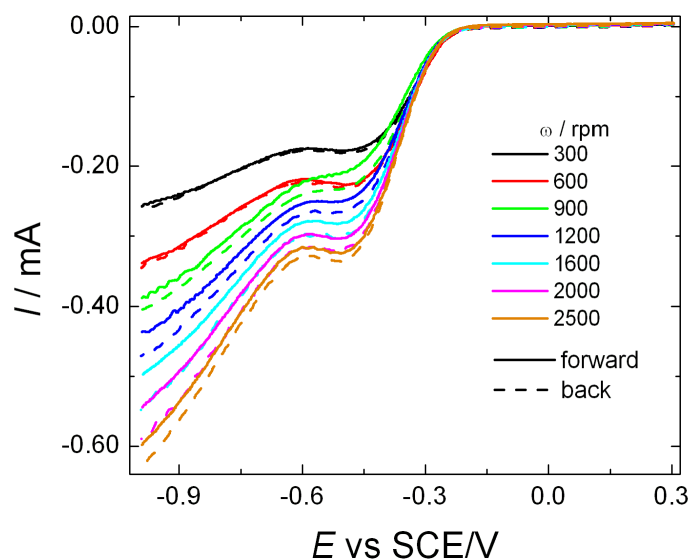

Figure S24. Hydrodynamic voltammetry curves obtained in O_2-saturated 0.1 M $HClO_4$ for O_2 reduction on a GC electrode surface-modified with 8 µg cm^{-2} of CCG. ν = 10 mV s^{-1}. Scans start at −0.75 V.
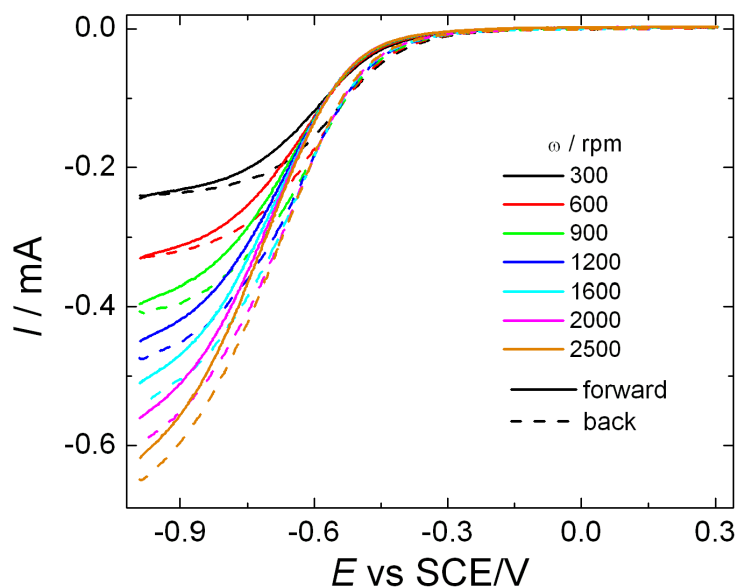
Figure S25. Hydrodynamic voltammetry curves obtained in O_2-saturated 0.1 M KH_2PO_4 (pH 7.0) for O_2 reduction on a GC electrode surface-modified with 8 μg cm^{-2} of GO. ν = 10 mV s^{-1}. Scans start at -1.0 V.
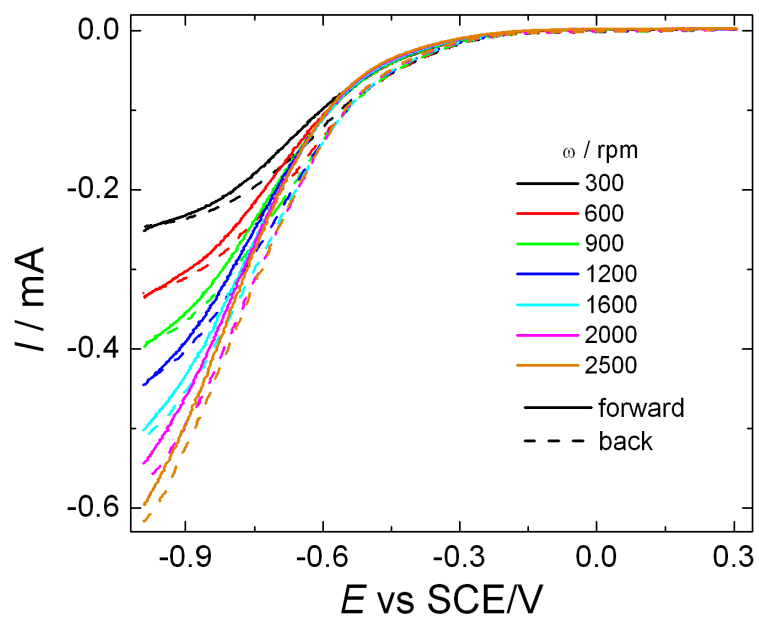
Figure S26. Hydrodynamic voltammetry curves obtained in O_2-saturated 0.1 M KH_2PO_4 (pH 7.0) for O_2 reduction on a GC electrode surface-modified with 8 μg cm^{-2} of CCG. ν = 10 mV s^{-1}. Scans start at -1.0 V.

Figure S27. Hydrodynamic voltammetry curves obtained in O_2-saturated 0.1 M KOH for O_2 reduction on a GC electrode surface-modified with 8 μg cm^{-2} of GR. $v = 10$ mV s^{-1}. Scans start at -1.0 V.
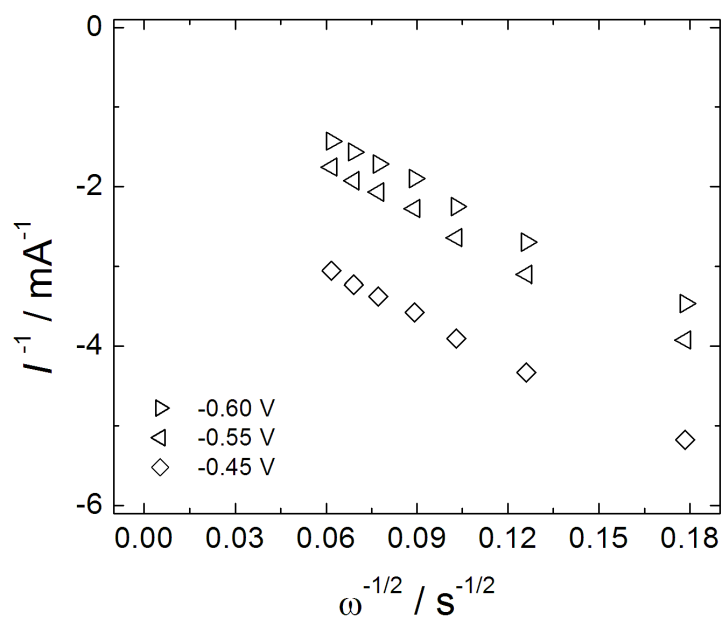

Figure S28. Hydrodynamic voltammetry curves obtained in O_2-saturated 0.1 M KOH for O_2 reduction on a GC electrode surface-modified with 8 μg cm^{-2} of GO. $v = 10$ mV s^{-1}. Scans start at -1.0 V.

Figure S29. Hydrodynamic voltammetry curves obtained in O_2-saturated 0.1 M KOH for O_2 reduction on a GC electrode surface-modified with 8 μg cm^{-2} of CCG. ν = 10 mV s^{-1}. Scans start at −1.0 V.

Figure S30. Koutecký–Levich plots obtained using back potential scan for O_2 reduction on a bare GC electrode in O_2-saturated 0.1 M HClO$_4$ (data from Figure S22).
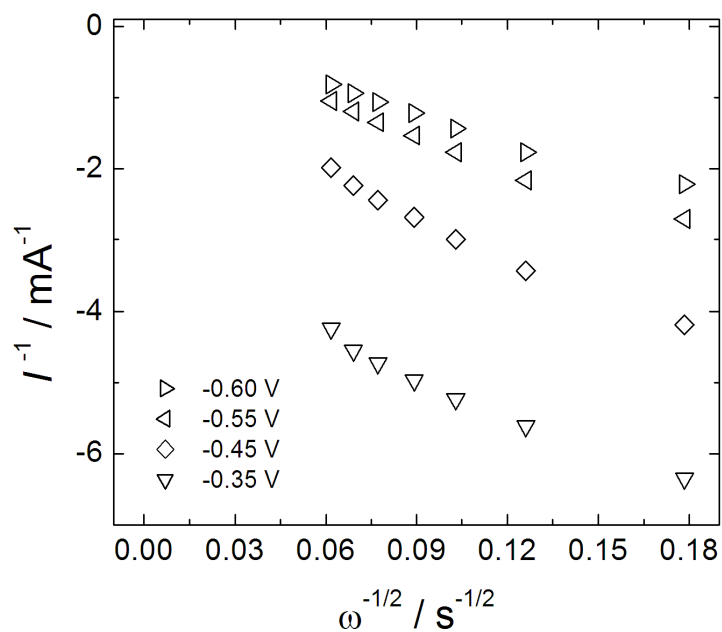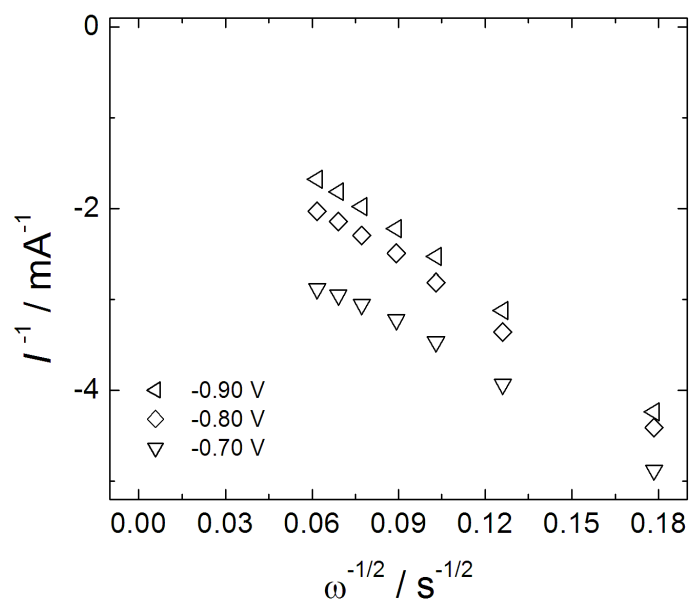
Figure S31. Koutecký–Levich plots obtained using back potential scan in O_2-saturated 0.1 M $HClO_4$ for O_2 reduction on a GC electrode surface-modified with 8 µg cm^{-2} of GO (data from Figure S23).
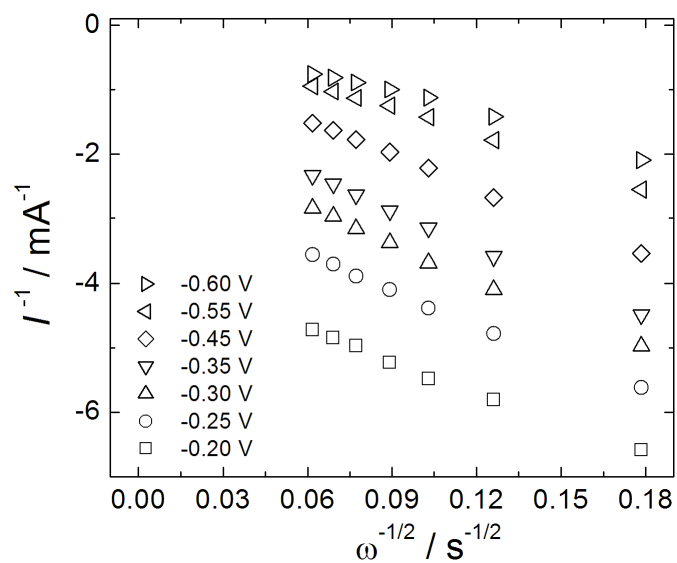
Figure S32. Koutecký–Levich plots obtained using back potential scan in O_2-saturated 0.1 M $HClO_4$ for O_2 reduction on a GC electrode surface-modified with 8 µg cm^{-2} of CCG (data from Figure S24).
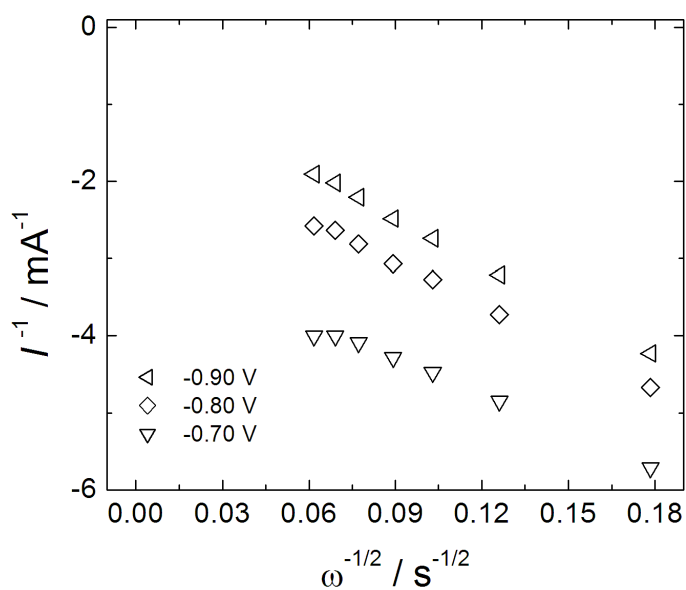
Figure S33. Koutecký–Levich plots obtained using back potential scan in O_2-saturated 0.1 M KH_2PO_4 (pH 7.0) for O_2 reduction on a GC electrode surface-modified with 8 µg cm^{-2} of GO (data from Figure S25).

Figure S34. Koutecký–Levich plots obtained using back potential scan in O_2-saturated 0.1 M KH_2PO_4 (pH 7.0) for O_2 reduction on a GC electrode surface-modified with 8 µg cm^{-2} of CCG (data from Figure S26).
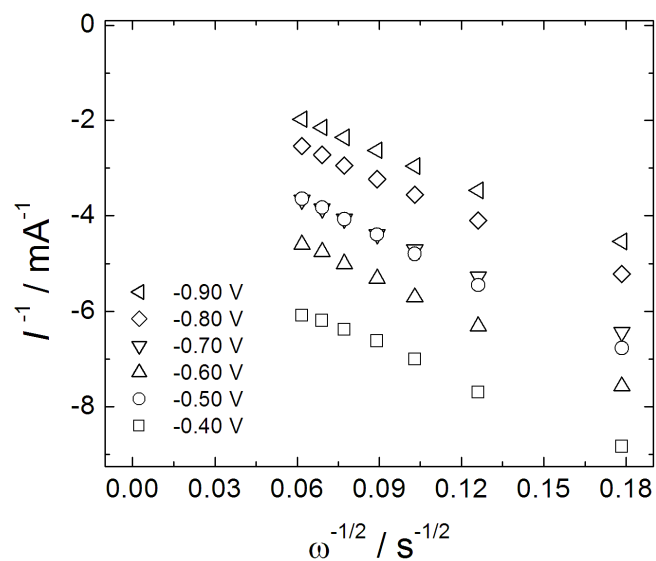
Figure S35. Koutecký–Levich plots obtained using back potential scan in O_2-saturated 0.1 M KOH for O_2 reduction on a GC electrode surface-modified with 8 μg cm^{-2} of GR (data from Figure S27).
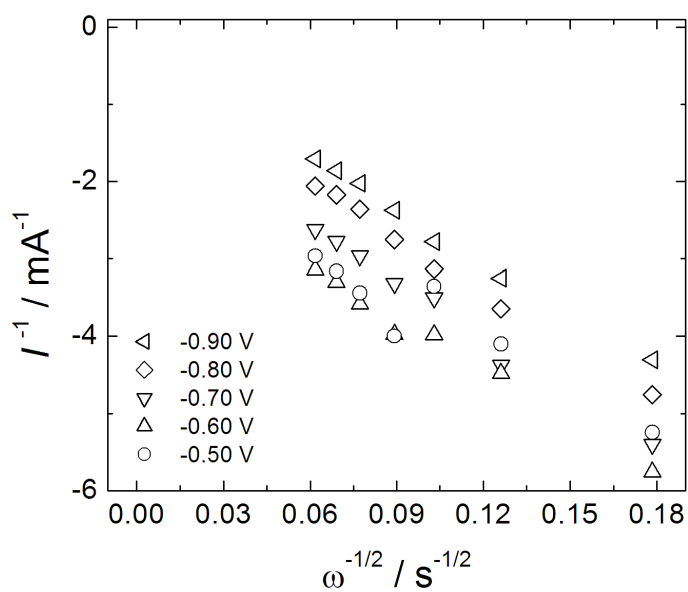
Figure S36. Koutecký–Levich plots obtained using back potential scan in O_2-saturated 0.1 M KOH for O_2 reduction on a GC electrode surface-modified with 8 μg cm^{-2} of GO (data from Figure S28).
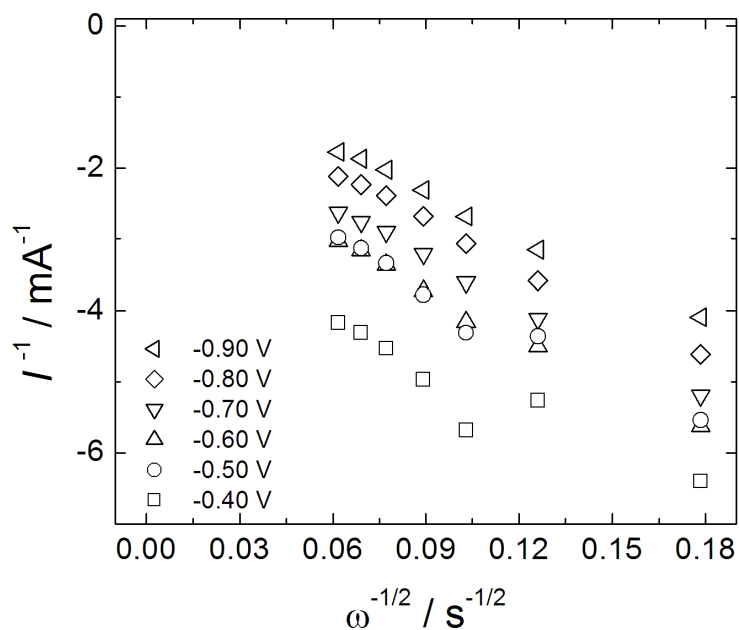
Figure S37. Koutecký–Levich plots obtained using back potential scan in O_2-saturated 0.1 M KOH for O_2 reduction on a GC electrode surface-modified with 8 μg cm^{-2} of CCG (data from Figure S29).
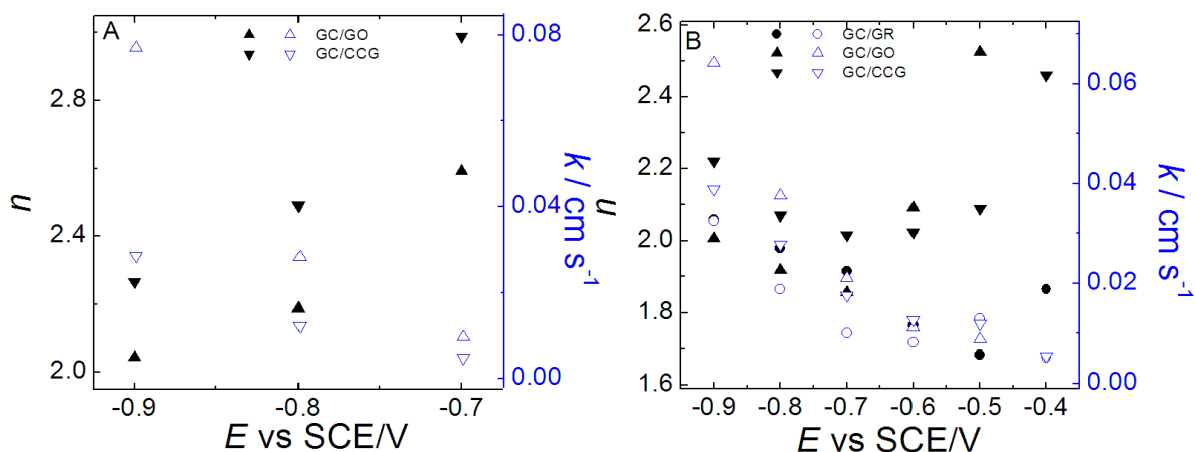

Figure S38. n and k vs. E plots obtained from data in Figures S33-S37 for O_2 reduction on GC electrodes surface-modified with 8 μg cm^{-2} of GR or GO, or CCG, in O_2-saturated 0.1 M KH$_2$PO$_4$ (pH 7.0) (A) and 0.1 M KOH (B).
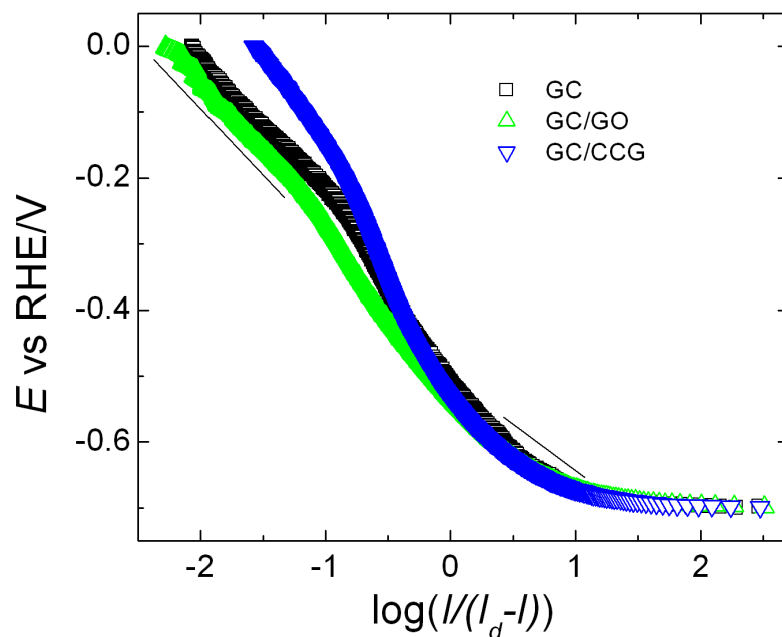
Figure S39. Tafel curves drawn from data in Figures S22-S24 for hydrodynamic voltammetric curves obtained at 1600 rpm. Lines indicate the regions used to determine Tafel inclinations at low and high polarizations (currents).

Figure S40. Tafel curves drawn from data in Figures S25-S26 for hydrodynamic voltammetric curves obtained at 1600 rpm. Lines indicate the regions used to determine Tafel inclinations at low and high polarizations (currents).

Figure S41. Tafel curves drawn from data in Figures S27-S29 for hydrodynamic voltammetric curves obtained at 1600 rpm. Lines indicate the regions used to determine Tafel inclinations at low and high polarizations (currents).
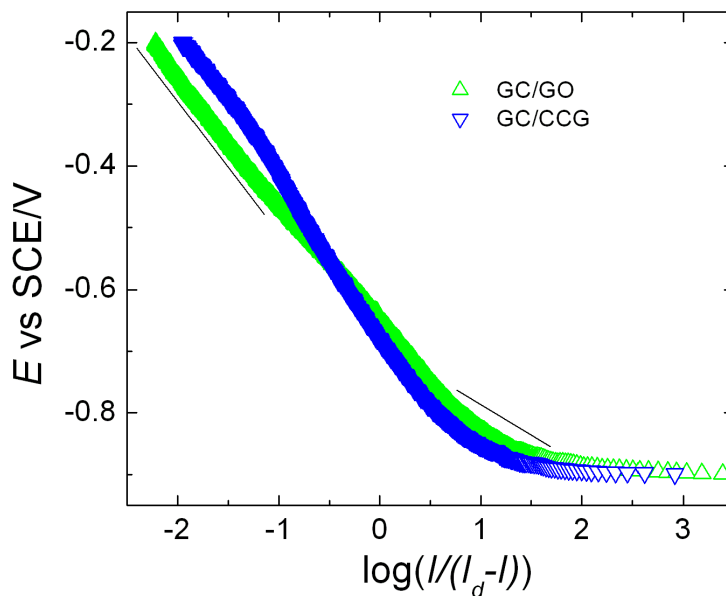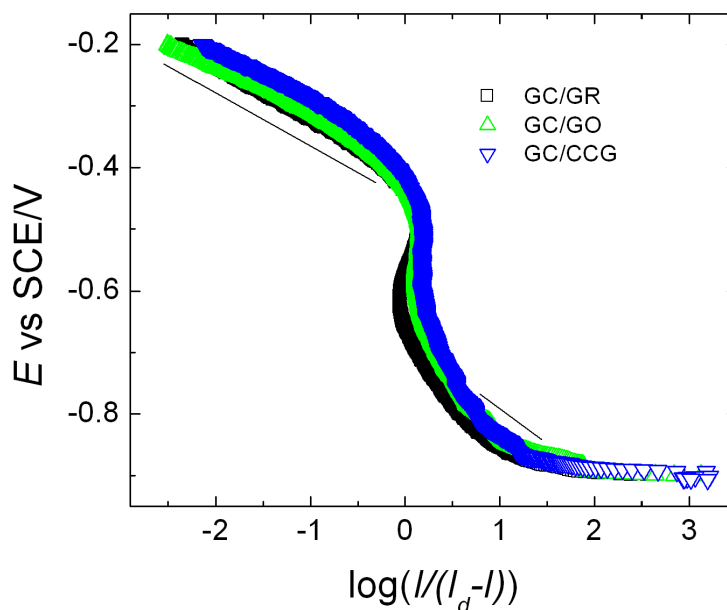
References

1 Y.Xu, H. Bai, G. Lu, C. Li and G. Shi, *J. Am. Chem. Soc.,*2008,**130**, 5856–5857.

2 W. S. Hummers Jr. and R. E. Offeman, *J. Am. Chem. Soc.,*1958, **80**, 1339.

3 N. I. Kovtyukhova, P. J. Ollivier, B. R. Martin, T. E. Mallouk, S. A. Chizhik, E. V. Buzaneva and A. D. Gorchinskiy, *Chem. Mater.,*1999, **11**, 771–778.

4 D. Li, M. B. Müller, S. Gilje, R. B. Kaner and G. G. Wallace, *Nat. Nanotechnol.,*2008,**3**, 101–105.

5 J. I.Paredes, S. Villar-Rodil, P. Solís-Fernández, A. Martíınez-Alonso and J. M. D. Tascón, *Langmuir,*2009,**25**,5957–5968.

6 S. Stankovich, D. A. Dikin, R. D. Piner, K. A. Kohlhaas, A. Kleinhammes, Y. Jia, Y. Wu, S.B. T. Nguyen and R. S. Ruoff, *Carbon,*2007, **45**, 1558–1565.

7 I. K. Moon, J. Lee, R. S. Ruoff, H. Lee, *Nat. Commun.,*2010, **1**, doi:10.1038/ncomms1067.

8 H.-L.Guo, X.-F. Wang, Q.-Y. Qian, F.-B. Wang and X.-H. Xia, *ACS Nano,*2009, **3**,2653–2659.

9 D. C.Marcano, D. V. Kosynkin, J. M. Berlin, A. Sinitskii, Z. Sun, A. Slesarev, L. B. Alemany, W. Lu and J. M. Tour, *ACS Nano,*2010, **4**,4806–4814.

10 Y.Zhou, G. Zhang, J. Chen, G. Yuan, L. Xu, L. Liu and F. Yang, *Electrochem. Commun.,*2012,**22**, 69–72

11 D. Chen, H. Feng and J. Li, *Chem. Rev.*2012,**112**, 6027-6053.

12 M. Acik, G. Lee, C. Mattevi, M. Chhowalla, K. Cho and Y. J. Chabal, *Nat. Mat,* 2010, **9,** 840-845.

13 M. J. Allen, V. C. Tung and R. B. Kaner, *Chem. Rev.,*2010**, 110***,* 132–145.

14 S. Park and R. S. Ruoff, *Nat. Nanotechnol.*, 2009, **4**, 217-224.

15 S. Stankovich, D. A. Dikin, G. H. B. Dommett, K. M. Kohlhaas, E. J. Zimney, E. A. Stach, R. D. Piner, S.B. T. Nguyen and R. S. Ruoff, *Nature,*2006,**442**, 282–286.

16 D. R. Dreyer, S. Park, C. W. Bielawski and R. S. Ruoff, *Chem. Soc. Rev.,*2010, **39**, 228–240.

17 O. C. Compton and S.B. T. Nguyen, *Small,*2010, **6**, 711–723.

18 A. J. Bard and L. R. Faulkner, *Electrochemical Methods: Fundamentals and Applications*, 2nd ed., John Wiley & Sons, Inc.: New York, 2001.

19 S. J. Konopka and B. McDuffie, *Anal. Chem.*1970,**42**, 1741–1746.

20 L. B.Venarusso, K. Tammeveski and G. Maia, *Electrochim. Acta,*2011, **56**, 8926–8933.

21 S. R.Santos and G. Maia, *Electrochim. Acta,*2012,**71**, 116–122.

22 A. H. H.Tanji, F. Lima, S. R. Santos and G. Maia, *J. Phys. Chem. C,*2012, **116,** 18857–18864.